Applied Energy 263 (2020) 114618

Contents lists available at ScienceDirect

Applied Energy

journal homepage: www.elsevier.com/locate/apenergy

Wound field synchronous motor with hybrid circuit for neighborhood electric vehicle traction improving fuel economy

Kyoung-Soo Cha, Dong-Min Kim, Young-Hoon Jung, Myung-Seop Lim*

Department of Automotive Engineering, Hanyang University, Seoul 04763, Republic of Korea

HIGHLIGHTS

- A method is proposed to improve the fuel economy of a neighborhood electric vehicle.
- A schematic of hybrid circuit and a method to decide mode change speed are proposed.
- The hybrid circuit increased the motor efficiency by up to 14%.
- The hybrid circuit improved the fuel economy of the vehicle by up to 3.8%.

GRAPHICAL ABSTRACT

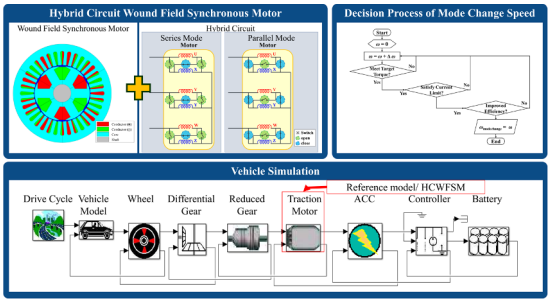

ARTICLE INFO

Keywords:
Electric vehicle
Fuel economy
Hybrid circuit
Vehicle simulation
Wound field synchronous motor

ABSTRACT

Increasing the low mileage associated with electric vehicles is a major requirement. Improving the efficiency of the traction motor is one solution to solve the mileage problem. In this study, we propose a method to improve the efficiency of a wound field synchronous motor (as the traction motor) in case of neighborhood electric vehicles. The wound field synchronous motor is a salient pole machine that generates a negative reluctance torque when operating in the second quadrant, reducing its efficiency. However, second quadrant operation is inevitable due to voltage limitation in the high-speed range. Here, we propose a hybrid circuit comprising U, V, W windings and X, Y, Z windings. The high-speed efficiency of the wound field synchronous motor is improved by changing the connection between the windings. Further, a neighborhood electric vehicle with a wound field synchronous motor was simulated using an advanced vehicle simulator (ADVISOR) to verify the proposal. The hybrid circuit increased the fuel economy of the electric vehicle by up to 3.8%. Finally, a validation experiment was conducted using a fabricated motor prototype.

1. Introduction

1.1. Motivation

The interest in eco-friendly vehicles, such as electric vehicles (EVs), has recently increased owing to the sanctions against the internal combustion engine (ICE) vehicles [1,2]. In EVs, the fuel tank and engine of the ICE vehicle are replaced by a battery and motor. These changes simplify the vehicle structure; additionally, the vibration and noise of the vehicle are considerably reduced. However, the EV batteries take a long time to fully recharge and exhibit low energy densities. Therefore, researchers intend to increase the mileage capabilities of the EVs by reducing the energy consumption and increasing their efficiency.

The reduction of the energy consumption of EVs has been approached from several perspectives, including energy management strategy, topology suggestion, and components improvement. Energy

* Corresponding author.
E-mail address: myungseop@hanyang.ac.kr (M.-S. Lim).

https://doi.org/10.1016/j.apenergy.2020.114618
Received 29 September 2019; Received in revised form 22 December 2019; Accepted 4 February 2020
Available online 12 February 2020

management provides energy management strategies based on the connection between the vehicle and the cloud [3,4], whereas topology-based studies have combined multi-motor and multi-speed transmission [5,6]. The component-based approaches attempt to reduce the energy consumption by optimizing various design parameters, such as the gear ratio [7,8], or by improving the powertrain efficiency [9,10]. In this study, we propose a method that can reduce the energy consumption by improving the efficiency of the traction motor, which powers the EV powertrain.

The automotive industry requires high-efficiency, high-speed, and high-power density motors to increase the mileage capabilities of the EVs. Various motors, including surface-mounted permanent magnet synchronous motors (SPMSMs), interior permanent magnet synchronous motors (IPMSMs), induction motors, wound field synchronous motors (WFSMs), and synchronous reluctance motors, are being studied as traction motors for use in EVs. However, the most suitable type of traction motor is IPMSM [11,12]. IPMSMs generally use rare earth magnets; however, such magnets are susceptible to volatile changes in market price [13]. Therefore, academia and industry continue to study non-rare-earth magnet motors [14,15]. Hence, WFSMs are also being researched [16]. The WFSM exhibits a high-power density because it uses magnetic torque and reluctance torque like an IPMSM. Also, for high-speed operations, IPMSMs only achieve flux-weakening control, whereas WFSMs achieve flux-weakening control and field-weakening control. Therefore, WFSMs have a higher degree of freedom (DOF) with respect to the control method, enabling effective high-speed operations. Hence, WFSMs are being researched as a traction motor for EVs.

1.2. Previous research

Recent studies of WFSMs have discussed design and control methods. A previous study [17] proposed permanent magnet-assisted WFSM (PMA–WFSM) to improve the efficiency. References [18,19] changed the shape of the WFSM to improve efficiency, and references [20,21] analyzed the effects of iron loss in the WFSM. Some studies [22,23] proposed a control method that operates more efficiently than the maximum torque per ampere control method. Furthermore, some studies [24,25] proposed brushless WFSM (BLWFSM) without slip rings and brushes, which are considered to be the disadvantages of WFSM.

1.3. Contribution

The objective of this study is to increase the fuel economy of EVs by improving the efficiency in the high-speed operating region of the WFSM. During high-speed operations, field-weakening control and flux-weakening control are achieved owing to voltage limitations; therefore, WFSM operates inefficiently in the second quadrant. Therefore, we propose a hybrid circuit that reduces the induced voltage by changing the number of series turns per phase for efficient high-speed operation. Also, the schematic of a hybrid circuit and the decision process of the mode change speed for a hybrid circuit are proposed. The efficiency improvement after the application of the hybrid circuit to the WFSM is confirmed via a two-dimensional (2D) finite element analysis (FEA). In addition, the effectiveness of the applied method is investigated by comparing the fuel economies of a WFSM-powered vehicle with and without the hybrid circuit by a vehicle simulation study. The previously obtained results of the 2D FEA of the hybrid circuit WFSM (HC WFSM) is reflected in the vehicle simulation. Therefore, HC WFSM can effectively improve the fuel efficiency. The originality of this study is shown in Fig. 1. In summary, the originality is as follows:

- For better fuel economy of EV, the method to improve motor efficiency is proposed.
- The schematic of the proposed method and the decision process of mode change speed are suggested.
- Fuel economy improvement of EV is confirmed through the vehicle simulation.

1.4. Structure

This study proposes a hybrid circuit to improve the efficiency of WFSMs in high-speed operating regions and confirms the effect of the proposed method on the vehicle fuel economy. First, we discuss the behavior of WFSMs when they are exposed to high-speed operating conditions; subsequently, we discuss how and why a hybrid circuit is proposed to solve inefficient operation in high-speed condition. The improvement in the efficiency of WFSM using a hybrid circuit was confirmed via FEA, and the cause was analyzed. Next, a vehicle simulation was performed for the same driving cycle and neighborhood electric vehicle (NEV) based on the efficiency map of the HC WFSM calculated via 2D FEA. The vehicle simulation was performed using an advanced vehicle simulator (ADVISOR) developed by the National Renewable Energy Laboratory (NREL) [26]. Finally, the validity of this study is confirmed via experiments using HC WFSM.

2. WFSM for NEV

2.1. Reference model

In this section, information regarding the reference model that satisfies the target performance of a traction motor for an NEV is introduced. WFSM is the motor type of the reference model for NEV traction. A detailed description of the WFSM is provided in the next section. The number of poles and slots of the reference model is 6 and 36, respectively. Distributed winding is the winding method of the reference model. The coil pitch is 5 coil spans, indicating short-pitch winding, and the air-gap length of the reference model is 0.5 mm. The core material used for the rotor and stator is 35PN230, which exhibits a thickness of 0.35 mm. The iron loss is 230 W/kg when exposed to the 1.0 T magnetic field with 50 Hz frequency. The number of series turns per phase and parallel circuits of the armature winding is 48 and 1, respectively, and the number of turns per pole of field winding is 300. The maximum torque and power of the reference model are 20 Nm and 4.2 kW, respectively. Further, the base speed and maximum speed of the reference model are 2000 and 9000 rpm, respectively. The information used within the reference model has been summarized in Table 1. Fig. 2 shows the characteristic curve of the reference model. As shown in Fig. 2, the reference model satisfies all the target performance while simultaneously satisfying the given constraints.

2.2. Feature of WFSM

As mentioned previously, WFSM is the motor type of the reference model, and the configuration of the reference model is presented in Fig. 3. As shown in Fig. 3, the best feature of the WFSM is that the field flux is generated by the field coil. Therefore, WFSM has a higher DOF of controllability than that possessed by a permanent magnet synchronous motor (PMSM) because field-weakening control can be achieved only by controlling the field current. Another important feature of the WFSM is that the d-axis inductance is larger than the q-axis inductance, unlike that observed in the PMSMs; examples include IPMSMs and SPMSMs. Generally, the torque of synchronous motors is represented by (1) using d, q-axis equivalent circuit. As shown in (1), WFSM can generate a positive reluctance torque (the second term in the square bracket on the right side of (1)) only during first-quadrant operation in which a positive d-axis current is applied. In (1), T_M is the motor torque, P_n is the number of pole pair, L_f is the field inductance, L_d is the d-axis inductance, L_q is the q-axis inductance, i_f is the field current, i_d is the d-axis current, and i_q is the q-axis current. The case in which a positive d-axis current is applied can be referred to as the first-quadrant operation. Conversely, in the second-quadrant operations, where a negative d-axis current is applied, a negative reluctance torque is generated. Therefore,

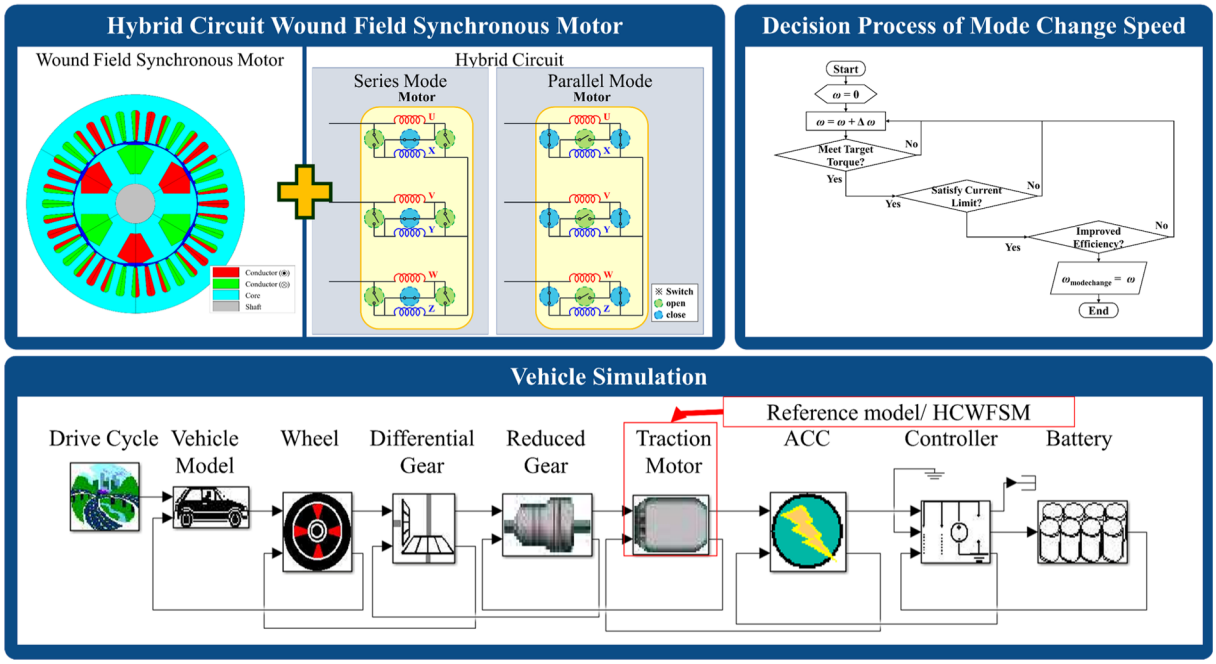

Fig. 1. Originality of this study.

Table 1
Information of the reference model.

	Unit	Value
The number of poles	–	6
The number of slots	–	36
Coil pitch	–	5
Air-gap length	mm	0.5
The number of series turns per phase	–	48
The number of parallel circuit	–	1
The number of field turns per pole	–	300
Core material	–	35PN230
Maximum torque	Nm	20
Maximum power	kW	4.2
Base speed	RPM	2000
Maximum speed	RPM	9000

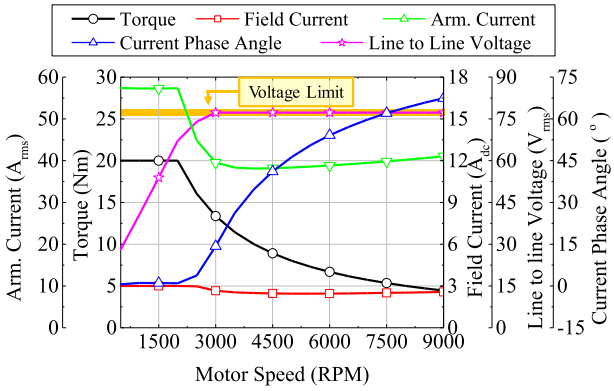

Fig. 2. Characteristic curve of reference model.

WFSMs should be operated in the first quadrant to ensure efficient operation. Table 2 presents the torque characteristics of the WFSM according to the operating region, and Fig. 4 shows the vector diagrams of the first- and second-quadrant operations.

$$T_M = P_n[L_f i_f i_q + (L_d - L_q) i_d i_q] \quad (1)$$

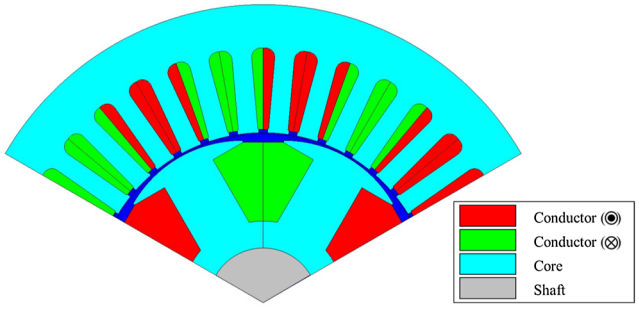

Fig. 3. Configuration of reference model.

Table 2
Torque characteristics of the WFSM according to the operation region.

Operation region	Magnetic Torque	Reluctance Torque
1st quadrant	+	+
2nd quadrant	+	−

2.3. Disadvantage of WFSM

As previously mentioned, the magnitude of the field flux can be altered by controlling the magnitude of the field current because the field flux of the WFSM is produced by the field current, unlike the PMSMs in which the magnitude of the field flux cannot be controlled. Therefore, WFSMs can increase the operating range using field-weakening control, which decreases the field flux by reducing the field current in the high-speed region. However, in the reference model, the field current does not significantly decrease even when the voltage is saturated, as shown in Fig. 2. Instead, the current phase angle is remarkably increased by applying flux-weakening control. Further, it has to be ensured that the voltage limit is not exceeded. This means that a negative *d*-axis current is applied and that the WFSM is operating in the second quadrant. When the WFSM is operated in this manner, the magnetic torque should be increased to satisfy the target torque because of the production of negative reluctance torque. Therefore, the *q*-axis current must be increased to increase the magnetic torque. Hence, the

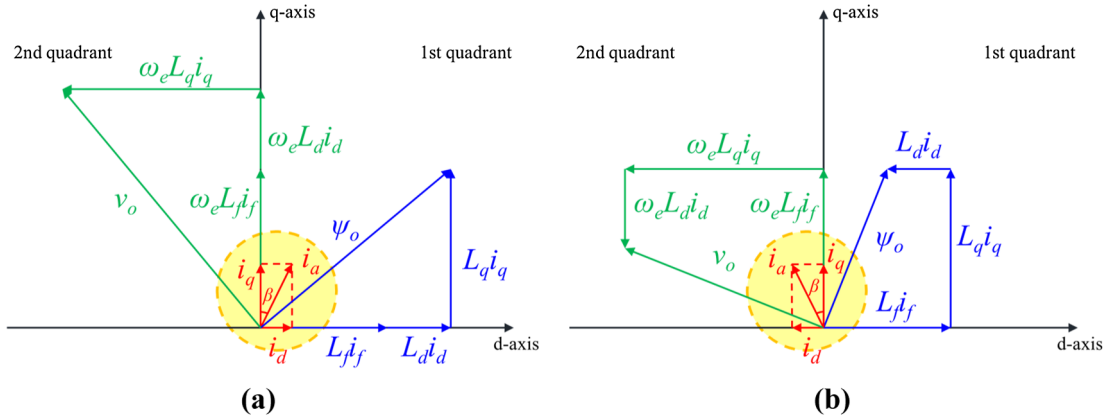

Fig. 4. Vector diagrams of the 1st and 2nd quadrant operation (a) 1st quadrant operation (b) 2nd quadrant operation.

WFSM efficiency is decreased due to the increment of copper loss. Because this phenomenon worsens with an increase in the rotational speed, this problem should be considered to be solved. In this study, the operating method of HC WFSM is proposed to solve this problem [27].

3. Hybrid circuit wound field synchronous motor

3.1. Concept of HC WFSM

In this section, the HC WFSM concept is described, which is used to solve the problem mentioned in Section 2.3. An HC WFSM has two windings per phase, and the connection method between the two windings is dependent upon the modes. The modes are divided into three types: series, single, and parallel modes. The series mode connects the two windings in series and is the winding connection method utilized in the reference model presented in this study. In the single mode, only one of the two windings is used, and the number of turns of the two windings can be either identical or different. In the parallel mode, both the windings are connected in parallel, and the number of turns of the two windings must be identical to prevent the occurrence of circulating current because of the resistance difference of two windings.

The HC WFSM winding connections are converted from the series mode to the single mode or parallel mode and vice versa at a certain rotational speed. In this study, when the HC WFSM is converted from the series mode to the single mode, it is called a "series–single mode HC WFSM," whereas when the HC WFSM is converted from the series mode to the parallel mode, it is called a "series–parallel mode HC WFSM". By assuming that the three phases of the first and second windings comprise U, V, W and X, Y, Z, respectively, the circuits for the series–single mode HC WFSM and the series–parallel mode HC WFSM are presented in Fig. 5. The converting circuit, shown in Fig. 5, is the simplest circuit without considering the additional safety circuits required to prevent drastic change of the voltage and current in the transient state during mode conversion. As shown in Fig. 5, the number of switching elements in the converting circuit from the series mode to the single mode is less than that in the converting circuit from the series mode to the parallel mode.

When the winding connection is converted from the series mode to the single mode or parallel mode, all the electrical parameters and characteristics change because of the decrease in the number of series turns per phase. The magnitudes of electrical parameters, including the phase resistance of the armature winding, the field flux linkage, and the *d*- and *q*-axis inductances, are related with the number of series turns per phase and are given by (2)–(4), respectively. Here, R_a is the armature phase resistance, N_s is the number of series turns per phase, l_c is the coil length, a is the number of parallel circuits, σ is the conductivity, and A_c is the cross-sectional area of the conductor. ψ_a is the linkage flux of the field, N_f is the number of field turns, and $R_{m,d}$ and $R_{m,q}$ are the magnetic reluctances along the *d*-axis and *q*-axis, respectively.

$$R_a = \frac{N_s l_c}{a\sigma A_c} \tag{2}$$

$$\psi_a = \frac{N_s N_f i_f}{R_{m,d}} \tag{3}$$

$$L_d = \frac{N_s^2}{R_{m,d}}, \quad L_q = \frac{N_s^2}{R_{m,q}} \tag{4}$$

Therefore, the magnitude of the electrical parameters after mode change is less than that before mode change. Because the input voltage of a WFSM is expressed as (5), the input voltage is reduced owing to the decrease in magnitude of the electrical parameters after mode change. In (5), v_o is line-to-line induced voltage and ω_e is the electrical angular velocity.

$$v_o = \omega_e \sqrt{(L_f i_f + L_d i_d)^2 + (L_q i_q)^2} \tag{5}$$

Therefore, the negative *d*-axis current can be decreased for flux-weakening control and efficient operation. However, the *q*-axis current is increased to satisfy the target torque because of the reduction in flux linkage by field. Therefore, copper loss decreases or increases depending on the armature current despite the reduction in the phase resistance of the armature winding after mode change.

3.2. Decision of mode change speed

As mentioned in Section 3.1, HC WFSM changes the mode at a certain rotational speed termed as the mode change speed. The mode change speed is determined based on the armature current, torque, and efficiency. First, the armature current should be less than the current limit for mode change to meet the target torque. Next, the mode change speed is determined at the point at which the efficiency begins increasing after mode change. The decision process of the mode change speed is presented in Fig. 6. In case of a series–single mode HC WFSM, the mode change speed is dependent on the number of series turns per phase of the single mode.

3.3. Characteristics change of HC WFSM after mode change

In this section, the characteristic differences between the HC WFSM and the reference model are described. The characteristic curve, *d*- and *q*-axis current, copper loss, efficiency, and input voltage of the HC WFSM and the reference model are compared. In this section, the series–parallel mode HC WFSM is compared with the reference model because the trend of changes in characteristics remains unchanged despite various combinations of the HC WFSM being used according to the mode. To obtain various characteristics, a non-linear

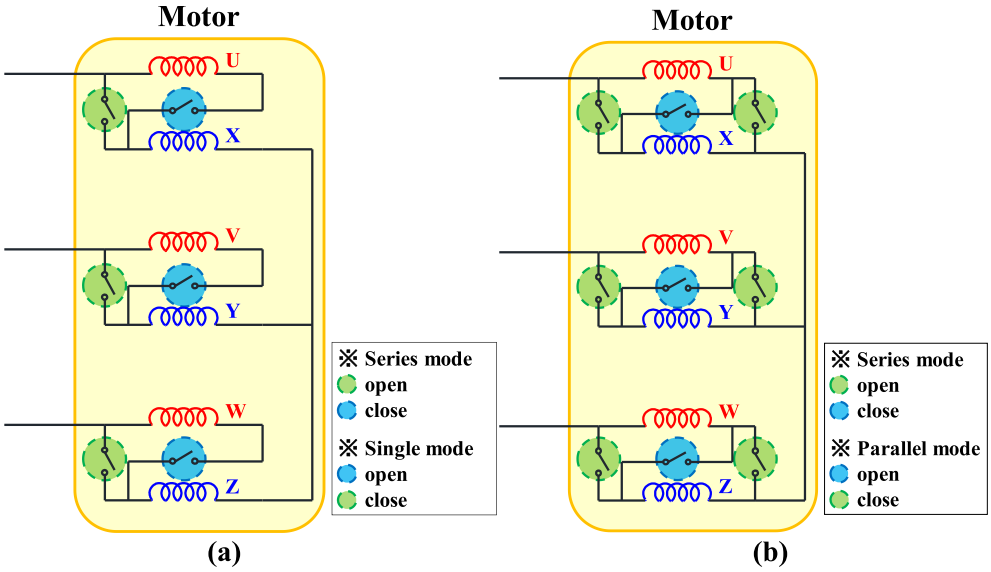

Fig. 5. Circuits for HC WFSM (a) series-single mode (b) series-parallel mode.

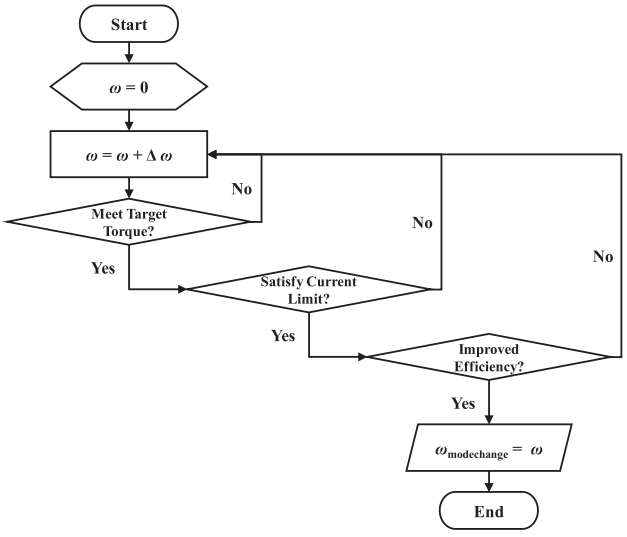

Fig. 6. Decision process of mode change speed.

electromagnetic field analysis was conducted using an in-house program similar to JMAG or MAXWELL in its functionality.

The characteristic curves of the HC WFSM and the reference model are presented in Fig. 7. As shown in Fig. 7(a), the current phase angle is increased to a value not exceeding the input voltage instead of the field current being reduced. Therefore, the reference model operates in the second quadrant and generates a negative reluctance torque. Accordingly, the *q*-axis current is increased to increase the magnetic torque for achieving the target torque. The increase in input current decreases the efficiency of the reference model. In case of the HC WFSM, the input voltage remarkably decreases after the mode change, and the current phase angle is reduced to almost 0°. The *q*-axis current is increased to achieve the target torque because the linkage flux by the field current is reduced; however, the efficiency is increased due to the reduction of the phase resistance of the armature winding. In addition, the field current is considerably reduced, improving the efficiency.

The *d* and *q*-axis currents of the HC WFSM and the reference model were also compared. As shown in Fig. 8, the negative *d*-axis current of the reference model increases as the rotational speed increases. In the HC WFSM, the *d*-axis current is almost 0 or is remarkably less when compared to that of the reference model. However, as mentioned earlier, the *q*-axis current of the HC WFSM is increased to achieve the target performance. These changes in current change the torque. As expected, after the mode change in the HC WFSM, the reluctance torque is almost 0, and the demanded magnetic torque is less when compared with that of the reference model. Therefore, it can be concluded that the HC WFSM exhibits efficient operation.

The armature copper loss in case of the HC WFSM and the reference

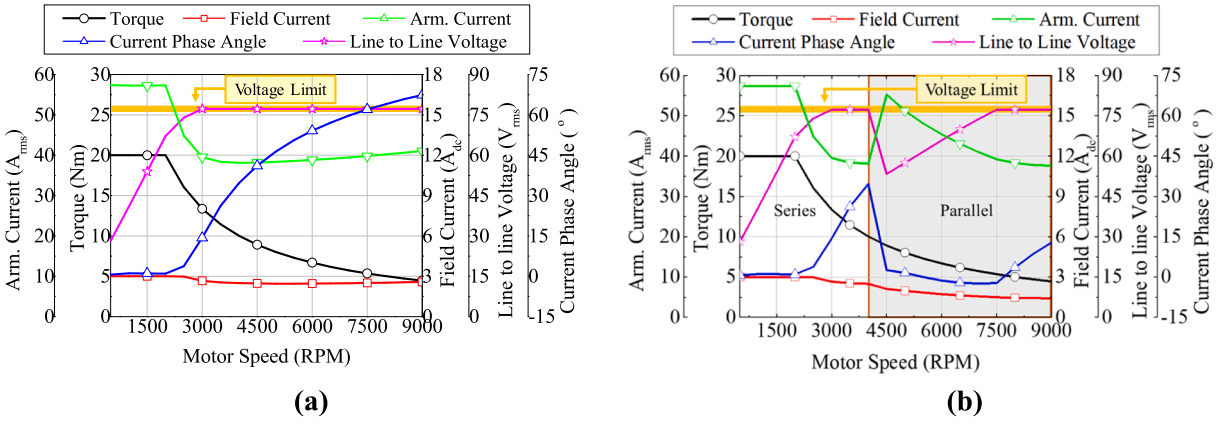

Fig. 7. Characteristic curves (a) reference model (b) HC WFSM.

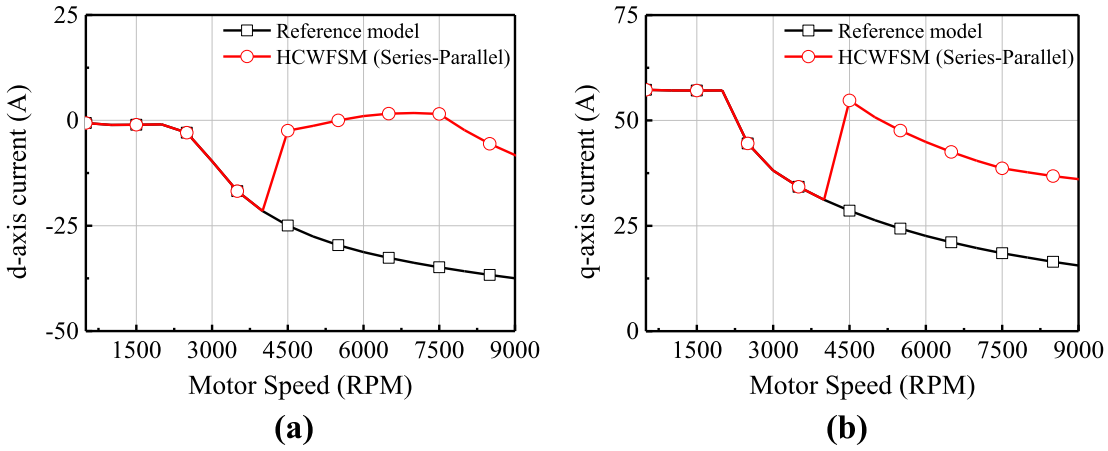

Fig. 8. *d-q* axis current (a) *d*-axis current (b) *q*-axis current.

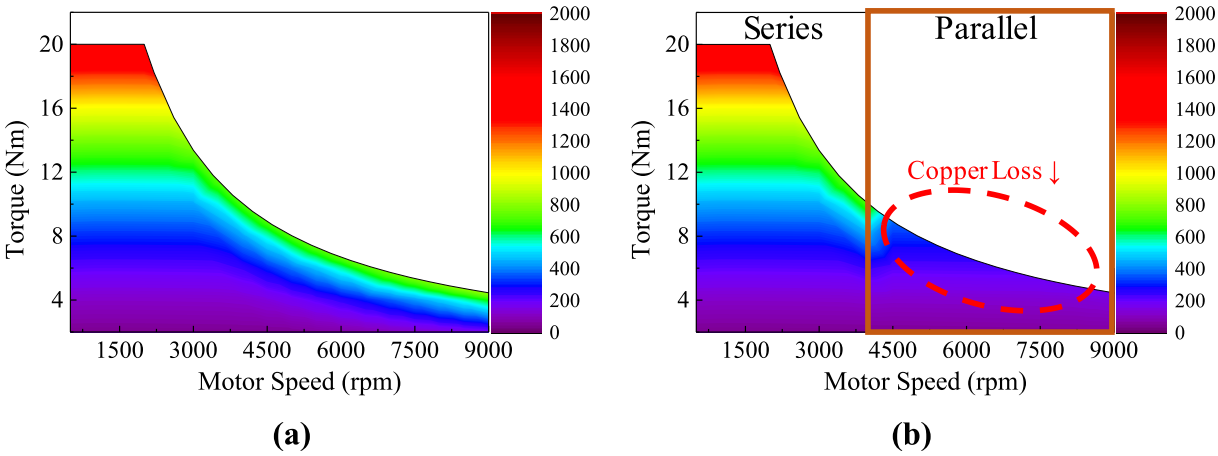

Fig. 9. Armature copper loss (a) reference model (b) HC WFSM.

model was also compared. The armature copper loss was considered for all the stator windings. As shown in Fig. 9, the HC WFSM reduces the armature copper loss when compared with the reference model because the armature resistance is reduced to 1/4 in the parallel mode. In the high-speed region, the armature copper loss is further reduced because the armature current is almost similar in both the models.

Fig. 10 shows the field copper loss of both the models. The field copper loss was investigated with respect to the HC WFSM and the reference model, and it was observed that the field copper loss decreased due to the decrease in field current after the mode change. The reduced field copper loss after mode change can be attributed to the reduction of the phase angle, ensuring that less field current was required to generate the same torque.

$$\eta_M = \frac{P_{out}}{P_{in}} = \frac{P_{out}}{P_{out} + P_{C,field} + P_{C,armature} + P_W} \tag{6}$$

Finally, the efficiencies of the HC WFSM and the reference model were compared. The efficiency is calculated using (6). In (6), η_M is the

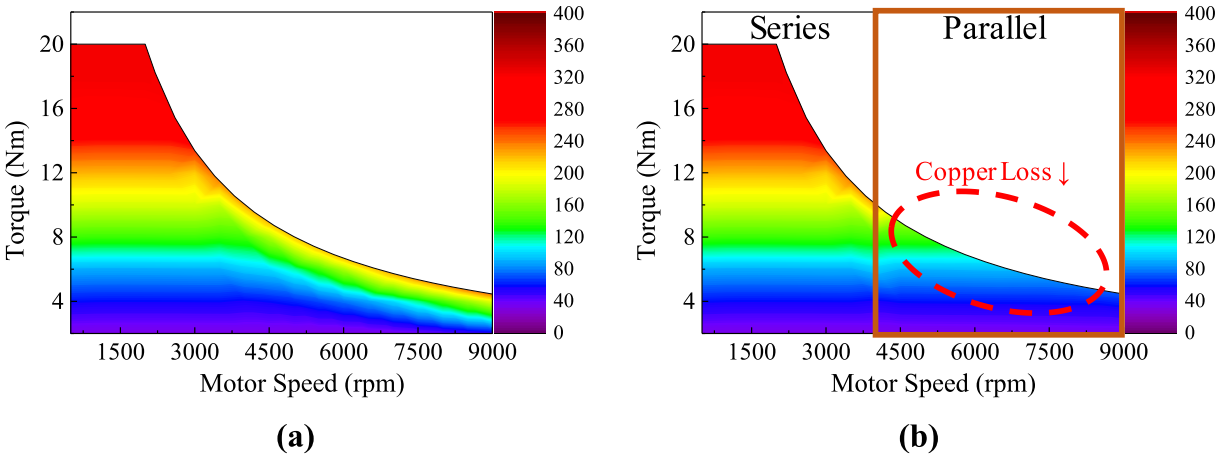

Fig. 10. Field copper loss (a) reference model (b) HC WFSM.

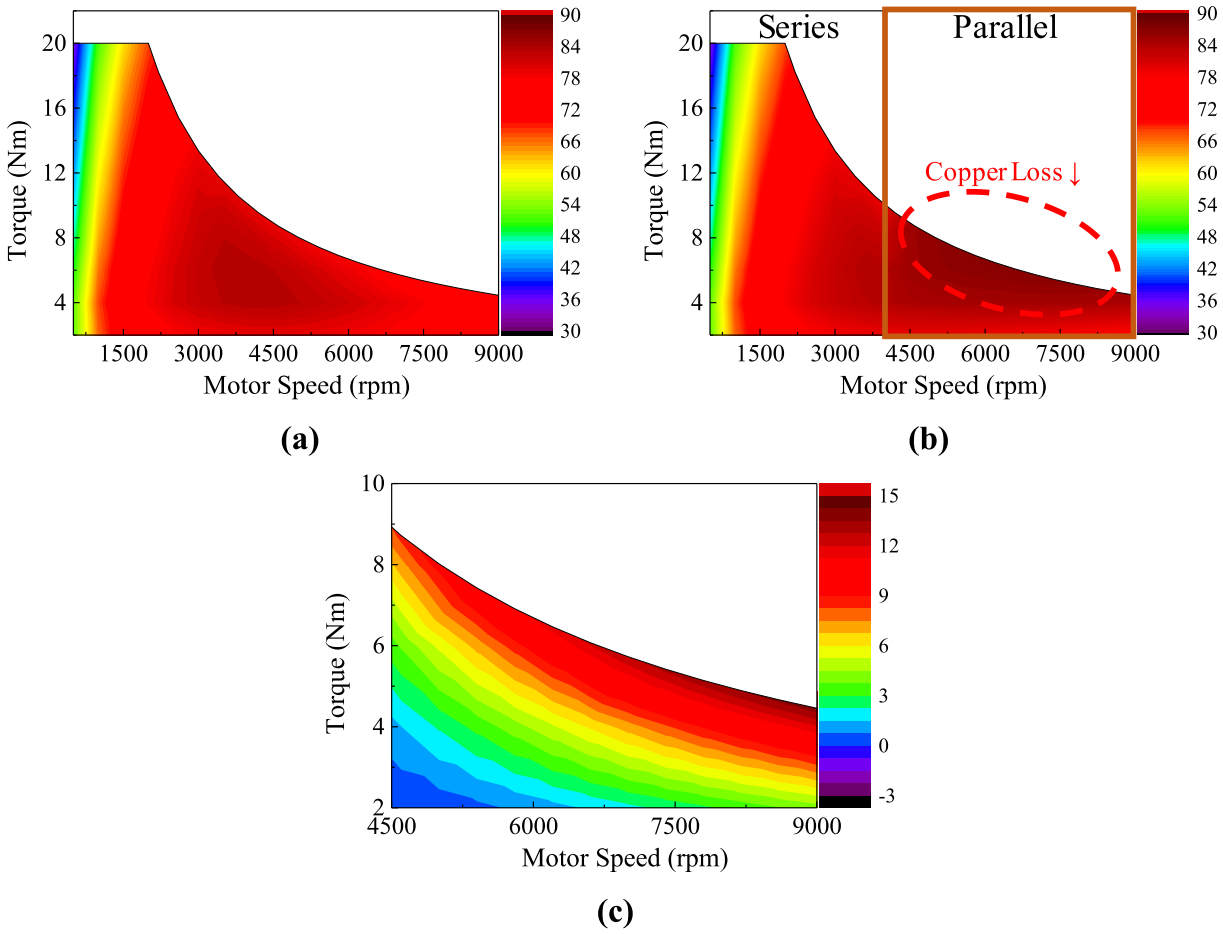

Fig. 11. Efficiency of motor (a) reference model (b) HC WFSM (c) efficiency difference of both model.

motor efficiency, P_{in} is the instantaneous input power of the motor, P_{out} is the instantaneous output power of the motor, $P_{C,field}$ is the field copper loss, $P_{C,armature}$ is the armature copper loss, and P_W is the iron loss. Fig. 11 shows the efficiency of the HC WFSM and the reference model. After the mode change, the overall efficiency was considerably improved by up to 14%. Furthermore, the higher the speed, the more noticeable will be the improvement in efficiency. Therefore, applying the HC to the WFSM for EV traction is expected to improve the fuel economy.

3.4. Efficiency comparison of HC WFSM according to the mode

Before comparing the efficiencies of each mode, more detail is required with respect to the single mode. HC changes the connection between the armature coils. In single mode, there are many combinations of coil 1, which is used after the mode change, and coil 2, which is unused after the mode change. Thus, the single mode indicates the relation (number of coil 1: number of coil 2). Because the number of coils in the reference model is 4, the possible combinations in single mode are (3:1), (2:2), and (1:3). In addition, the maximum torque varies depending on the number of coils; therefore, the three combinations exhibit different mode conversion speeds.

The efficiency of the HC WFSM was investigated in each mode. Fig. 12 shows the efficiency of the motor according to each mode. After mode change, the efficiency of the motor was improved as shown in Fig. 13. When compared with the efficiency of the reference model, the series–parallel mode exhibited a notable improvement in efficiency by up to 14%. For the series–single mode, (2:2) improved by up to 10%. However, in single mode, the efficiency partially reduced. Next, vehicle simulations were performed, analyzed, and compared using the reference model and the HC WFSM for the EV traction to investigate the fuel economy.

4. Vehicle simulation

Vehicle simulations were conducted to verify the fuel economy when the target vehicle had completed a given driving cycle [26,28]. Vehicle simulations were performed on the advanced vehicle simulator (ADVISOR) developed by the National Renewable Energy Laboratory (NREL). ADVISOR is a credible tool used by the researchers in many laboratories, institutes, and companies. Fig. 14 shows a schematic of the vehicle simulations. EV simulations require specifications of the target vehicle, efficiency maps of the traction motor, and specifications regarding the battery and selected driving cycle. Therefore, in this section, the vehicle simulation is explained in detail. Vehicle simulations were performed using the HC WFSM to verify the fuel efficiency according to the HC WFSM mode.

4.1. Operating point of traction motor

Fig. 15 presents a dynamic force diagram of the vehicle. The dynamic force is divided into the traction force and the resistance force. The total resistance force $F_{total\_resistance}$ combines the rolling and grading resistance forces (F_R and F_G, respectively) and the aerodynamic drag force F_D. It can be calculated as

$$F_{total\_resistance} = F_R + F_G + F_D = f_R M_v g \cos\theta + M_v g \sin\theta + \frac{1}{2}\rho A_F C_D (V_v + V_w)^2 \quad (7)$$

where $F_{total\_resistance}$ is the total resistance force, F_R is the rolling

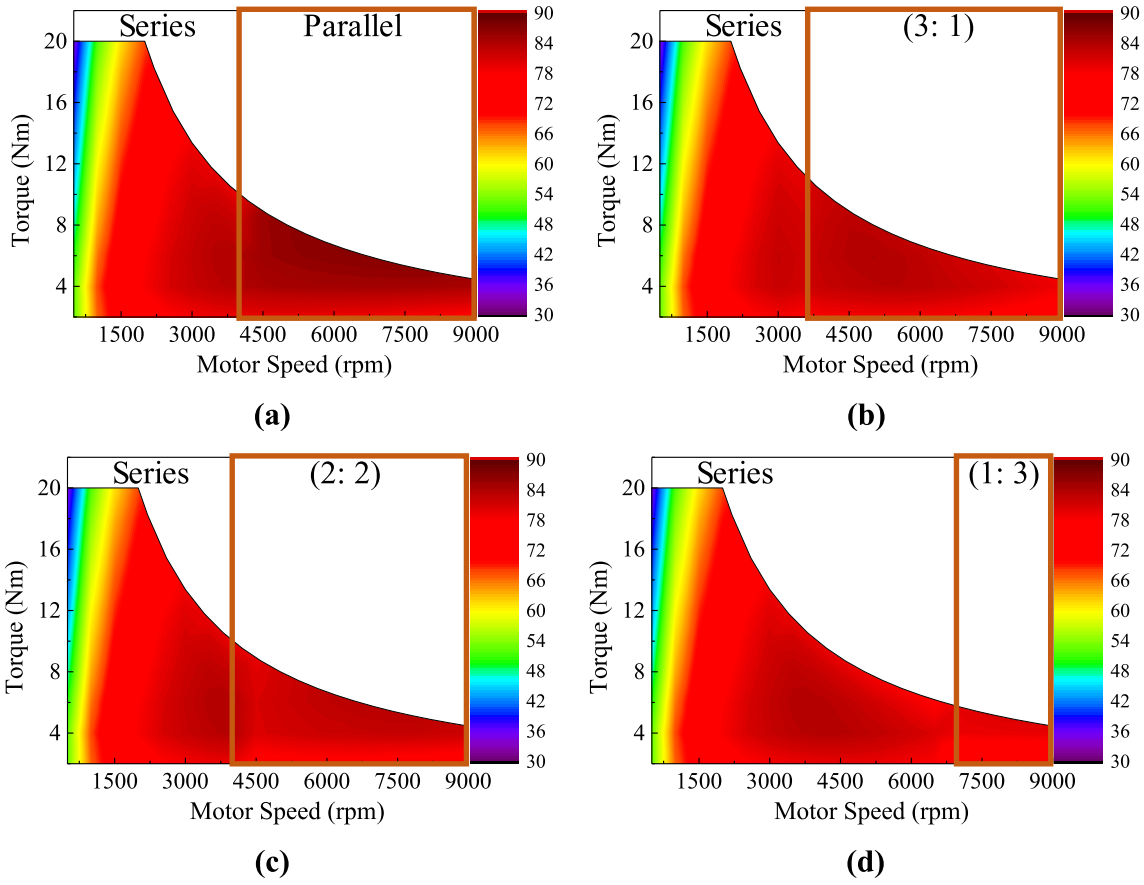

Fig. 12. Efficiency of HC WFSM (a) series-parallel (b) series-single (3:1) (c) series-single (2:2) (d) series-single (1:3).

resistance force, F_G is the grading resistance force, F_D is the aerodynamic drag force, f_R is the rolling resistance coefficient, M_v is the vehicle mass, g is the gravitational acceleration, θ is the longitudinal slope angle, and ρ is the air density. A_F is the frontal area of the vehicle, C_D is the aerodynamic drag coefficient, V_v is the vehicle speed, and V_w is the wind speed on the moving direction of the vehicle, which has a positive sign when this component is opposite to the vehicle speed and negative sign when it is in the same direction as the vehicle speed [29].

The traction and resistance forces determine the dynamic behavior of vehicle. The equation of motion can be given as follows:

$$M_v a = F_t - F_{total\_resistance} \tag{8}$$

Here, a is the acceleration of the vehicle and F_t is the traction force.

Because the vehicle simulation completes the target driving cycle, the operating point of the motor can be known based on the speed of the vehicle and the required traction. The required traction force for the driving target cycle can be given as follows:

$$F_t = M_v a + F_{total\_resistance} \tag{9}$$

The required torque of the motor is

$$T_M = \frac{r_w F_t}{n_G \eta_G} \tag{10}$$

where T_M is the required motor torque, r_w is the wheel radius, n_G is the gear ratio, and η_G is the gear efficiency.

The required speed of the motor is

$$N_M = \frac{60}{2\pi r_w} n_G V_v \tag{11}$$

where N_M is the required speed of the motor in revolution per minute (RPM).

4.2. Energy consumption model

The energy consumption is calculated based on the operating point of the motor by considering the efficiency of the motor and the inverter. In an EV, the motor performs acceleration and regenerative braking. Therefore, energy consumption must be calculated differently according to the motor operation. The instantaneous output power of the motor can be given as follows:

$$P_{out} = T_M \omega_M = T_M \frac{2\pi N_M}{60} \tag{12}$$

Here, P_{out} is the instantaneous motor output power and ω_M is the motor angular velocity.

The instantaneous input power of the motor according to the operation can be given as follows:

$$P_{in} = \begin{cases} \frac{P_{out}}{\eta_M \eta_{Inv}}, & T_M \geqslant 0 \\ P_{out} \eta_M \eta_{Inv}, & T_M < 0 \end{cases} \tag{13}$$

Here, P_{in} is the instantaneous input power of the motor, η_M is the motor efficiency, and η_{Inv} is the inverter efficiency.

The instantaneous input of the power of motor is integrated over time to obtain the total amount of energy consumption. The total amount of energy consumption can be given as follows:

$$E_C = \int P_{in} \mathrm{d}t \tag{14}$$

Here, E_C denotes the total amount of energy consumption.

4.3. Battery model

The main power source of an EV is its battery. The battery used for

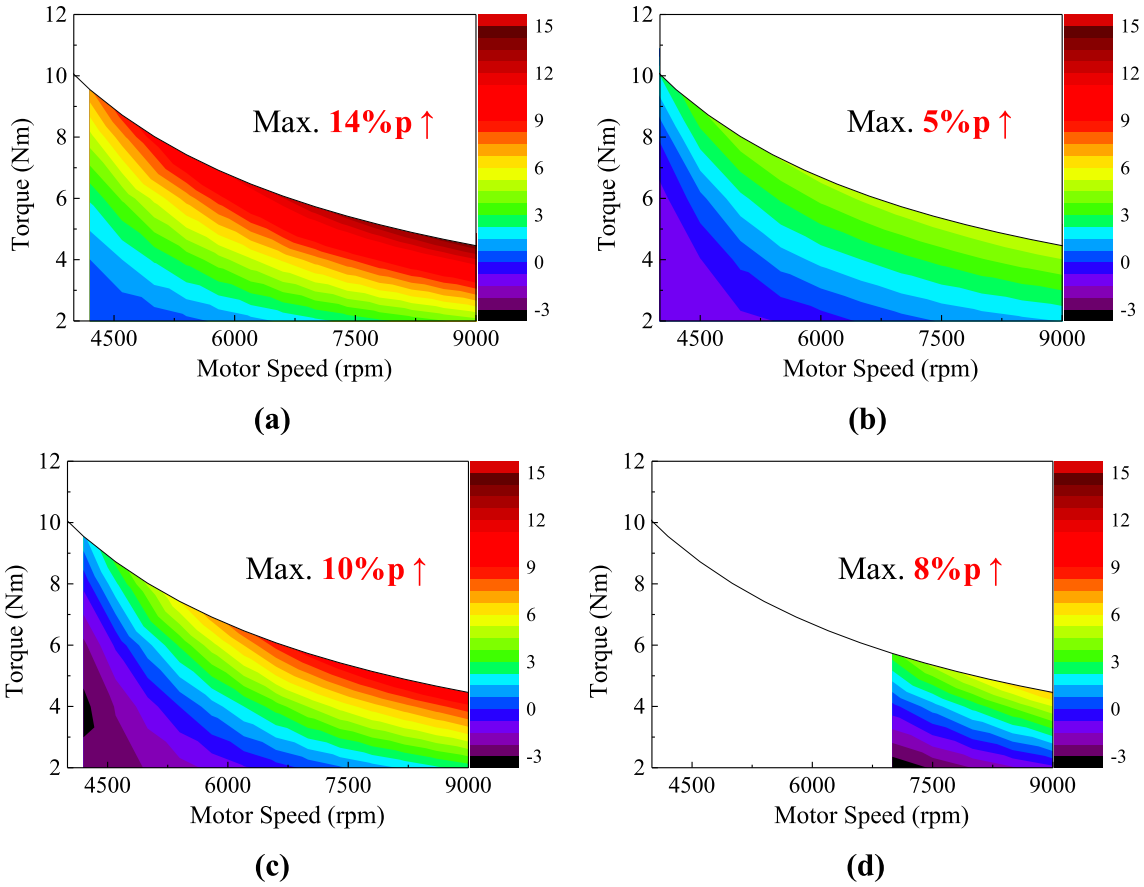

Fig. 13. Efficiency difference of HC WFSM and reference model (a) series-parallel (b) series-single (3:1) (c) series-single (2:2) (d) series-single (1:3).

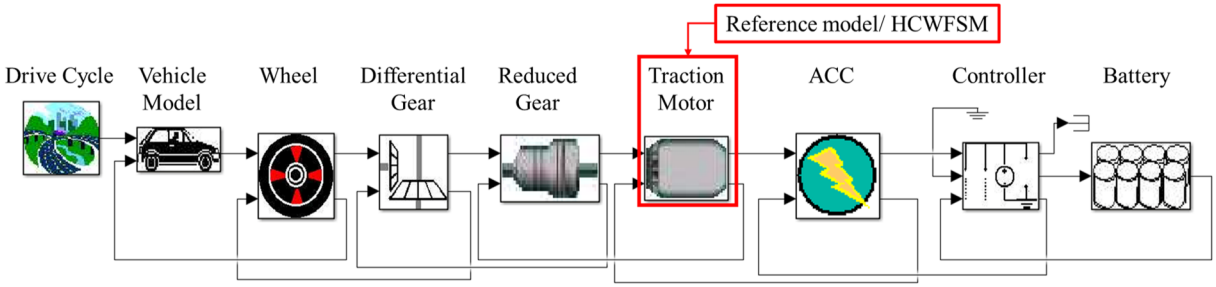

Fig. 14. Schematic of vehicle simulation.

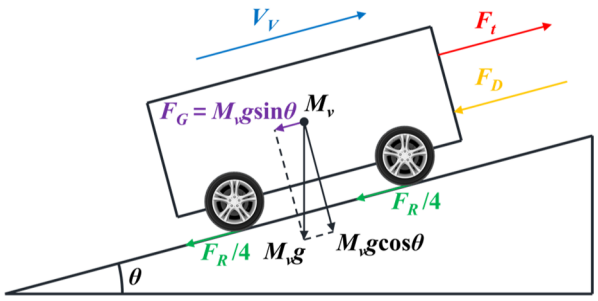

Fig. 15. Dynamic force diagram of the vehicle.

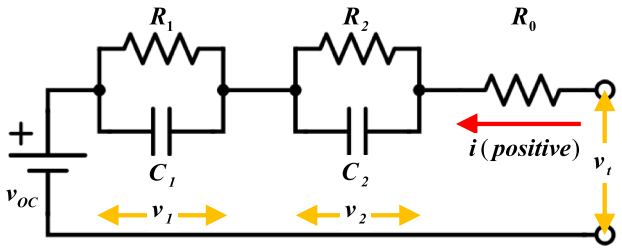

Fig. 16. Battery equivalent circuit.

the simulations is a lithium ion battery, which is commonly used in EVs. The used battery model was a second RC equivalent model and is shown in Fig. 16. Fig. 17 depicts the battery model parameter. This parameter was experimentally obtained [30–32]. The state-space model of the battery can be given as follows:

$$\frac{dSOC(t)}{dt} = \frac{i(t)}{C_{bat}} \tag{15}$$

$$\frac{dv_1(t)}{dt} = -\frac{v_1(t)}{R_1 C_1} + \frac{i(t)}{C_1} \tag{16}$$

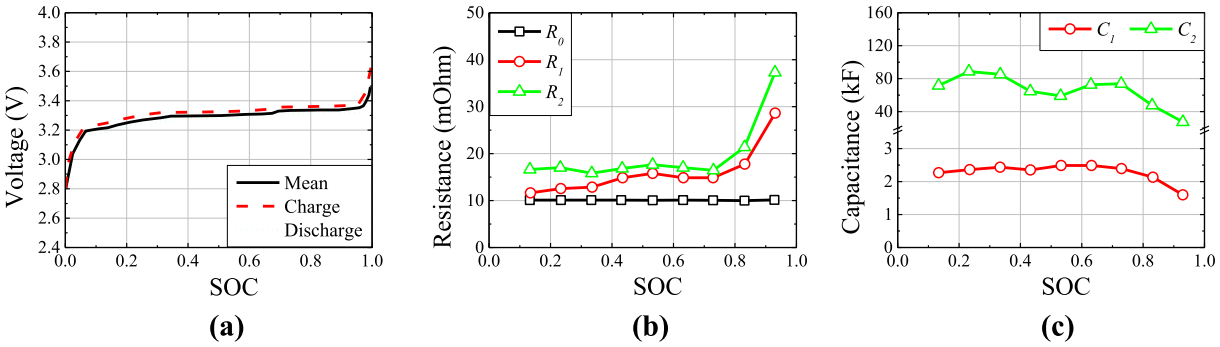

Fig. 17. Battery model parameter according to SOC (a) open circuit voltage (b) resistance (c) capacitance.

Table 3
Vehicle specification.

Items	Unit	Value
Curb weight	kg	474
Frontal area	m^2	1.8
Wheelbase	m	1.686
Wheel	mm	330
Gear ratio	–	9.23
Gear efficiency	%	95
Inverter efficiency	%	95
Battery capacity	kWh	6.1
Maximum speed	km/h	50

Table 4
Drive condition.

Items	Unit	Value
Air density	kg/m^3	1.2
Gravitational acceleration	m/s^2	9.81
Aerodynamic Drag Coefficient	–	0.64
Rolling Resistance Coefficient	–	0.01

$$\frac{dv_2(t)}{dt} = -\frac{v_2(t)}{R_2C_2} + \frac{i(t)}{C_2} \tag{17}$$

$$v_t(t) = v_{oc}(\mathrm{SOC}) + v_1(t) + v_2(t) + R_0 i(t) \tag{18}$$

Here, SOC denotes the state of charge, i is the current (positive for charging), C_{bat} is the nominal capacity of the battery, and R and C denote the resistance and capacitance, respectively. v_1 and v_2 are the voltages across the first and second capacitor, respectively, R_0 is the ohmic resistance, and v_t is the terminal voltage. R_1 and C_1 correspond to the first RC pair, whereas R_2 and C_2 correspond to the second RC pair.

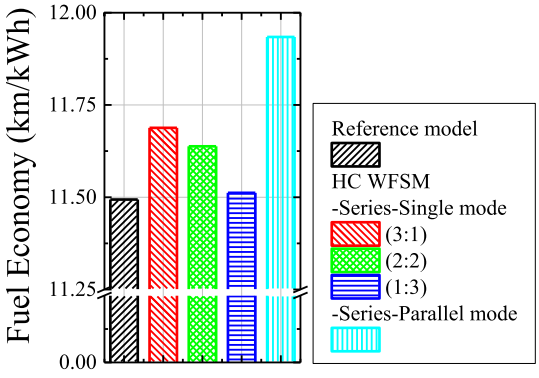

Fig. 19. Fuel economy of NEV.

4.4. Vehicle simulation condition

NEV is the target vehicle. Table 3 presents the vehicle specifications, and Table 4 presents the drive conditions. The aerodynamic drag coefficient and the vehicle specification are determined by referring Renault Twizy, and the rolling resistance coefficient was set by referring to previously conducted studies [33,34]. The inverter and gear were assumed to exhibit efficiencies of 95%. The efficiency map used by the traction motor model was obtained based on the modes in Figs. 11 and 12.

Fig. 18 shows the target driving cycle and the driving course shown on the map. The target driving cycle was created by referring to the existing ARP02. The driving cycle was modified to ensure that the

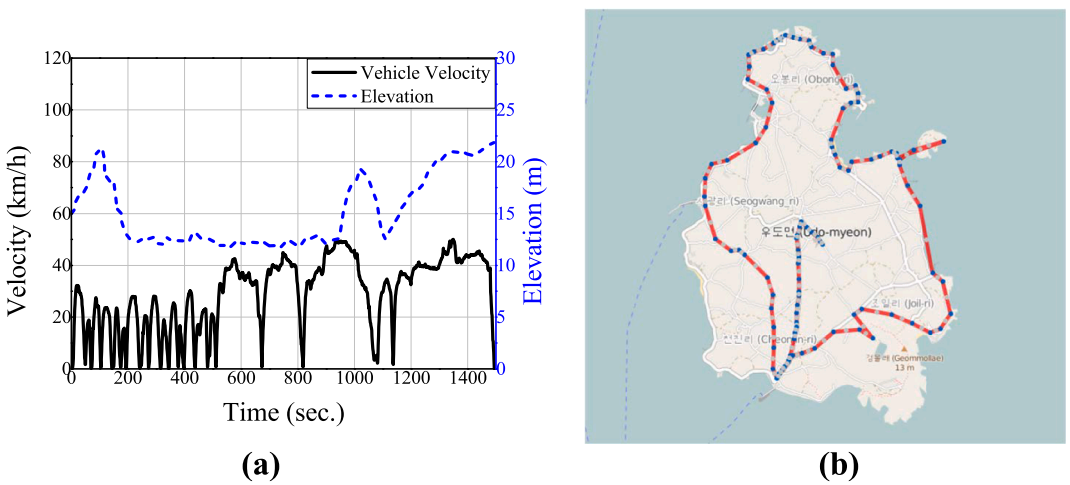

Fig. 18. Target driving cycle (a) target driving cycle (b) driving course shown on the map.

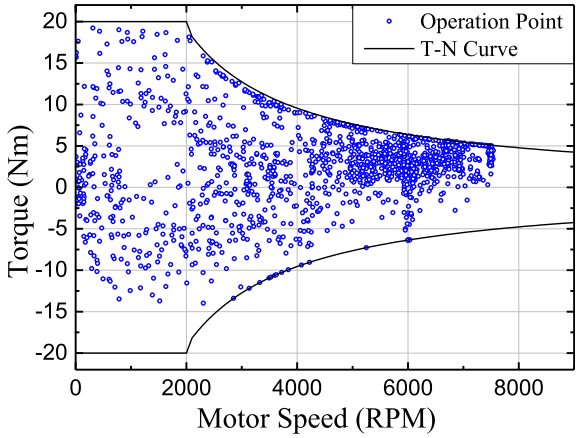

Fig. 20. Operation point of motor.

maximum speeds of the ARP02 and the target vehicle were identical. It also considered altitude by referring to the roads in Udo, South Korea. Udo was designated as an ecofriendly island, and NEVs were mostly used as rental cars.

4.5. Vehicle simulation result

Vehicle simulations were performed under the specifications and drive conditions of a real vehicle to confirm the effectiveness of the proposed method. Because only the characteristics of the motors differed in the vehicle simulations, we can confirm whether the proposed method increases the fuel efficiency by analyzing the vehicle simulation results.

Fig. 19 shows the fuel economy of the EV according to the HC WFSM mode. The fuel economy was the highest in the series–parallel mode of the HC WFSM and increased by 3.8% when compared with that of the original model. The series–single (3:1) mode increased the fuel economy by 1.7% when compared with the original model; however, the fuel economy increase rate was 2.1% lower than that in the series–parallel mode. The fuel efficiency was higher in the HC WFSM than that in the reference model, confirming that the proposed method effectively improves the fuel efficiency.

Fig. 20 denotes the operating points of the motor. The operating points of the motor are evenly distributed. The area in which the operating points are concentrated is approximately 4000 RPM or more and 7000 RPM or less. Therefore, increasing the motor efficiency in this area can reduce energy consumption.

Fig. 21 demonstrates a map denoting the influence of the operation point on efficiency. The series–parallel mode of the HC WFSM significantly improved the efficiency in all the areas after mode change. However, the series–single mode of HC WFSM exhibits an area in which the efficiency is reduced after mode change. The efficiency-improved area of the series–single mode is concentrated in case of high-speed operation and high torque. The efficiency is reduced in other areas. The efficiency-decreased area affects the decrease in fuel economy of the NEV. Therefore, the maximum increment in efficiency for (2:2) was 10%; however, the fuel economy was lower than (3:1). This is because many operating points were in the efficiency-decreased area for (2:2).

5. Experimental verification

The validity of the proposed method was confirmed via HC WFSM experiments. The turn ratio of the fabricated HC WFSM is (2:2) and can be tested in three modes: reference (4:0), series–parallel (2:2), and

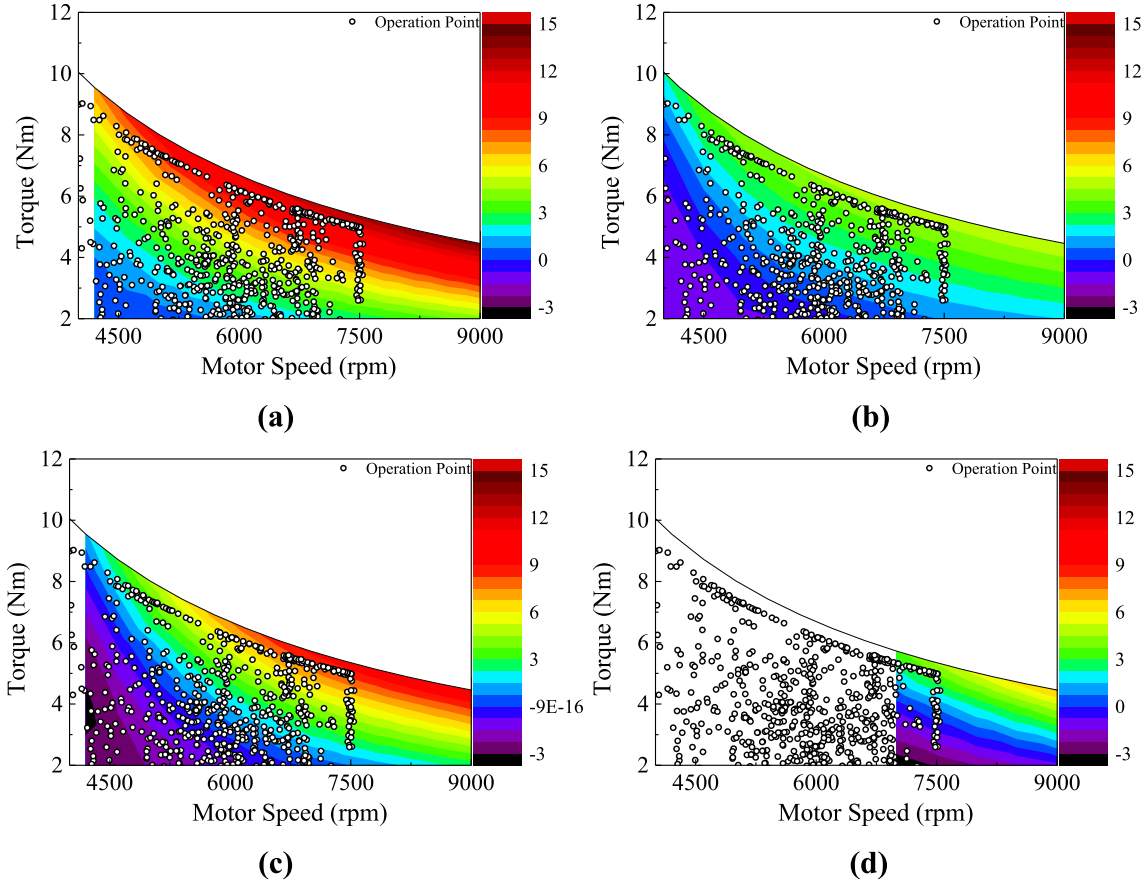

Fig. 21. Operation point on efficiency difference map (a) series-parallel (b) series-single (3:1) (c) series-single (2:2) (d) series-single (1:3).

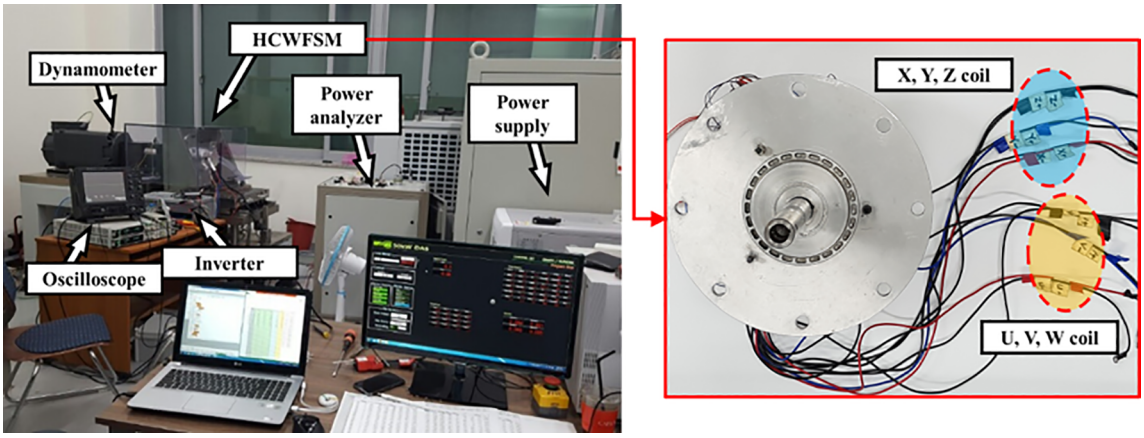

Fig. 22. Configuration of experiment and fabricated HC WFSM.

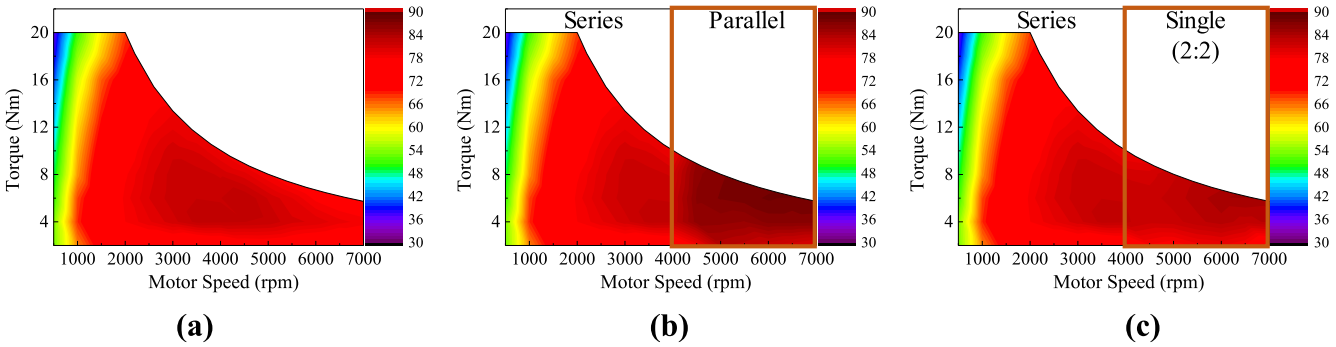

Fig. 23. Measured efficiency map (a) reference model (b) series-parallel (c) series-single (2:2).

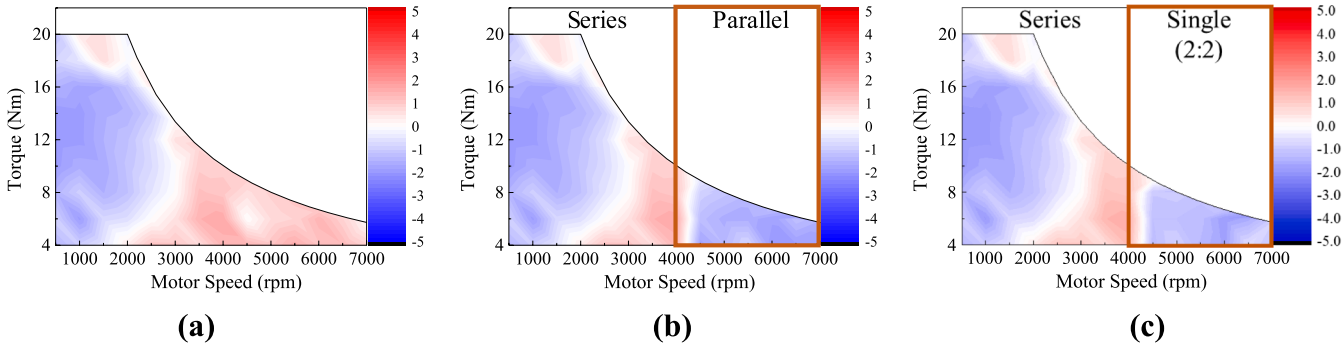

Fig. 24. Efficiency error between 2D-FEA and experiment (a) reference model (b) series-parallel (c) series-single (2:2).

series–single (2:2). The winding connection change during the experiment is not achieved automatically. Experiments were performed using the manual connections according to each mode.

Fig. 22 denotes the experimental configurations and the fabricated HC WFSM. The experiments required an inverter, a brake, a torque sensor, a speed sensor, and a power analyzer. The motor was driven using the current points obtained via *d,q* equivalent circuit based on 2D FEA results. The input power of the motor was calculated using the power analyzer, whereas the output power of the motor was calculated based on the measured torque and rotational speed. The calculated input and output powers were used to calculate the motor efficiency. The temperature of the motor was maintained at 40 °C because it affected the measurement of efficiency during the experiment.

Fig. 23 shows the efficiency map of the HC WFSM obtained via experiments, and Fig. 24 shows the efficiency error when comparing the simulations and experiments. The error between the two results was small, and the maximum error was approximately 2.0%. The enhanced motor efficiency after the application of the proposed method was validated based on the experimental results. In addition, the vehicle simulation results can be considered to be reliable based on the experimental results from the HC WFSM. Therefore, it can be indirectly demonstrated that the proposed method improves the NEV fuel efficiency without even conducting the vehicle test.

6. Conclusion

This study proposes a new method that can improve the fuel efficiency of an electric vehicle by changing the winding connection in a wound field synchronous motor. There are three winding connection modes: series, single, and parallel. The mode refers to the connection between windings 1 and 2 of the stator. The rotational speed at which the mode is changed is determined by the decision process of the mode speed change. The proposed method improved the efficiency of the electric motor by up to 14% in the series–parallel mode and by up to

10% in the series–single mode. In addition, when a wound field synchronous motor with a hybrid circuit was used as the traction motor, the fuel economy was improved by 3.8% and 1.7% in the series–parallel mode and the series–single mode, respectively. Finally, the proposed method and its simulated results were verified using an experiment. The experimental results only slightly differed from the simulation results; therefore, the results were considered to be reliable. Overall, the hybrid circuit improved the fuel efficiency of an electric vehicle powered using a wound field synchronous motor as the traction motor. In real vehicle applications, we must design a safety circuit that can avoid the danger caused by sudden parameter changes.

CRediT authorship contribution statement

Kyoung-Soo Cha: Conceptualization, Methodology, Software, Writing - original draft. **Dong-Min Kim:** Formal analysis, Software, Visualization. **Young-Hoon Jung:** Investigation, Methodology, Validation. **Myung-Seop Lim:** Supervision, Writing - review & editing.

Acknowledgment

This work was supported by the research fund of Hanyang University (HY-2019).

References

[1] Tu W, Santi P, Zhao T, He X, Li Q, Dong L, et al. Acceptability, energy consumption, and costs of electric vehicle for ride-hailing drivers in Beijing. Appl Energy 2019;250:147–60.
[2] Taljegard M, Göransson L, Odenberger M, Johnsson F. Impacts of electric vehicles on the electricity generation portfolio – A Scandinavian-German case study. Appl Energy 2019;235:1637–50.
[3] Hou J, Song Z. A hierarchical energy management strategy for hybrid energy storage via vehicle-to-cloud connectivity. Appl Energy 2020;257:113900.
[4] Qu X, Yu Y, Zhou M, Lin C-T, Wang X. Jointly dampening traffic oscillations and improving energy consumption with electric, connected and automated vehicles: A reinforcement learning based approach. Appl Energy 2020;257:114030.
[5] Kwon K, Seo M, Min S. Efficient multi-objective optimization of gear ratios and motor torque distribution for electric vehicles with two-motor and two-speed powertrain system. Appl Energy 2019:114190.
[6] Zhao M, Shi J, Lin C. Optimization of integrated energy management for a dual-motor coaxial coupling propulsion electric city bus. Appl Energy 2019;243:21–34.
[7] Gao B, Liang Q, Xiang Y, Guo L, Chen H. Gear ratio optimization and shift control of 2-speed I-AMT in electric vehicle. Mech Syst Signal Process 2015;50:615–31.
[8] Wang S, Chen K, Zhao F, Hao H. Technology pathways for complying with Corporate Average Fuel Consumption regulations up to 2030: A case study of China. Appl Energy 2019;241:257–77.
[9] Ding X, Guo H, Xiong R, Chen F, Zhang D, Gerada C. A new strategy of efficiency enhancement for traction systems in electric vehicles. Appl Energy 2017;205:880–91.
[10] Guo Q, Zhang C, Li L, Gerada D, Zhang J, Wang M. Design and implementation of a loss optimization control for electric vehicle in-wheel permanent-magnet synchronous motor direct drive system. Appl Energy 2017;204:1317–32.
[11] Ruuskanen V, Nerg J, Rilla M, Pyrhonen J. Iron loss analysis of the permanent-magnet synchronous machine based on finite-element analysis over the electrical vehicle drive cycle. IEEE Trans Ind Electron 2016;63(7):4129–36.
[12] Cha KS, Kim DM, Park MR, Yoon MH, Hong JP. Multipolar High-Speed IPMSM Design for EV Traction Considering Mechanical Stress. IEEE Veh. Technol. Conf. 2016. p. 1–6.
[13] Coey JMD. Perspective and Prospects for Rare Earth Permanent Magnets. Engineering 2019.
[14] Kim DM, Cha KS, Lim MS, Hong JP. Rare-earth-free electric motor design for ev traction comparing overall vehicle efficiency considering driving cycle. IEEE Veh. Technol. Conf. 2016. p. 1–5.
[15] Riba J-R, López-Torres C, Romeral L, Garcia A. Rare-earth-free propulsion motors for electric vehicles: A technology review. Renew Sustain Energy Rev 2016;57:367–79.
[16] Lee JJ, Lee J, Kim KS. Design of a WFSM for an electric vehicle based on a nonlinear magnetic equivalent circuit. IEEE Trans Appl Supercond 2018;28(3):1–4.
[17] Hwang SW, Sim JH, Hong JP, Lee JY. Torque improvement of wound field synchronous motor for electric vehicle by PM-assist. IEEE Trans Ind Appl 2018;54(4):3252–9.
[18] Park SI, Kim KC. Torque ripple reduction method with asymmetric pole for wound-field synchronous motor. IEEE Trans Magn 2015;51(3):1–4.
[19] Do SH, Lee BH, Lee HY, Hong JP. Torque ripple reduction of wound rotor synchronous motor using rotor slits. ICEMS 2012 - Proc. 15th Int. Conf. Electr. Mach. Syst. 2012. p. 1–4.
[20] Rasilo P, Belahcen A, Arkkio A. Importance of iron-loss modeling in simulation of wound-field synchronous machines. IEEE Trans Magn 2012;48(9):2495–504.
[21] Rasilo P, Belahcen A, Arkkio A. Experimental determination and numerical evaluation of core losses in a 150-KVA wound-field synchronous machine. IET Electr Power Appl 2013;7(2):97–105.
[22] Lee B-H. Design and maximum efficiency control of wound rotor synchronous machine for EV PhD. Thesis South Korea: Automotive Eng., Hanyang Univ.; 2013.
[23] Kim Y, Nam K. Copper-loss-minimizing field current control scheme for wound synchronous machines. IEEE Trans Power Electron 2017;32(2):1335–45.
[24] Di Gioia A, Brown I, Nie Y, Knippel R, Ludois D, Dai J, et al. Design and demonstration of a wound field synchronous machine for electric vehicle traction with brushless capacitive field excitation. IEEE Trans Ind Appl 2018;54(2):1390–403.
[25] Jawad G, Ali Q, Lipo TA, Il Kwon B. Novel brushless wound rotor synchronous machine with zero-sequence third-harmonic field excitation. IEEE Trans Magn 2016;52(7):1–4.
[26] Markel T, Brooker A, Hendricks T, Johnson V, Kelly K, Kramer B, et al. ADVISOR: a systems analysis tool for advanced vehicle modeling. J Power Sources Aug. 2002;110(2):255–66.
[27] Lim MS, Hong JP. Design of high efficiency wound field synchronous machine with winding connection change method. IEEE Trans Energy Convers 2018;33(4):1978–87.
[28] Kim DM, Benoliel P, Kim DK, Lee TH, Park JW, Hong JP. Framework development of series hybrid powertrain design for heavy-duty vehicle considering driving conditions. IEEE Trans Veh Technol 2019;68(7):6468–80.
[29] Ehsani M, Gao Y, Gay SE, Emadi A. Modern Electric, Hybrid Electric, and Fuel Cell Vehicles: Fundamentals, Theory, and Design. Boca Raton: CRC Press; 2010.
[30] Perez HE, Siegel JB, Lin X, Stefanopoulou AG, Ding Y, Castanier MP. Parameterization and Validation of an Integrated Electro-Thermal Cylindrical LFP Battery Model. 2012. p. 41–50.
[31] Perez HE. Model Based Optimal Control, Estimation, and Validation of Lithium-Ion Batteries Ph.D Thesis Berkeley, USA: Civil and Environmental Eng. Univ. of California; 2016.
[32] Klein M, Tong S, Park JW. In-plane nonuniform temperature effects on the performance of a large-format lithium-ion pouch cell. Appl Energy 2016;165:639–47.
[33] Renault U.K., Renault TWIZY. [Online]. Available: https://www.platinumrenault.co.uk/pdfs/new-cars/twizy.pdf. 2018.
[34] Tanujaya M, Lee DH, Ahn JW. Design a novel switched reluctance motor for neighborhoods electric vehicle. 8th Int. Conf. Power Electron. – ECCE Asia "Green World with Power Electron. ICPE 2011-ECCE Asia. 2011. p. 1674–81.